Optics & Laser Technology 181 (2025) 111849

Contents lists available at ScienceDirect

Optics and Laser Technology

journal homepage: www.elsevier.com/locate/optlastec

Full length article

A hybrid trans-modal liquid crystal optical vortex generator

A. Walewska [a], N. Bennis [a], T. Jankowski [a], P. Morawiak [a], D.C. Zografopoulos [b], M. Filipiak [c], M. Słowikowski [c], A. Cobo [d,e,f], J.F. Algorri [d,e,f,*]

[a] Faculty of Advanced Technologies and Chemistry, Military University of Technology, Warsaw 00-908, Poland
[b] Consiglio Nazionale delle Ricerche, Istituto per la Microelettronica e Microsistemi (CNR-IMM), Rome 00133, Italy
[c] The Centre for Advanced Materials and Technologies CEZAMAT, Warsaw University of Technology, 19 Poleczki St., 02-822 Warsaw, Poland
[d] Photonics Engineering Group, University of Cantabria, 39005, Santander, Spain
[e] CIBER de Bioingeniería, Biomateriales y Nanomedicina, Instituto de Salud Carlos III, 28029, Madrid, Spain
[f] Instituto de Investigación Sanitaria Valdecilla (IDIVAL), 39011, Santander, Spain

ARTICLE INFO

Keywords:
Optical vortices
Liquid crystals
Orbital angular momentum

ABSTRACT

This work experimentally validates a large-aperture optical vortex generator using a novel hybrid structure, combining transmission electrode and modal techniques, in what we term the trans-modal technique. The continuous transmission electrode is designed to generate a linear voltage distribution between the contact electrodes, while the electrode stubs distribute the voltage across the active area. A high-resistivity layer of the conducting polymer PEDOT fills the gap between the electrodes, resulting in a completely continuous voltage distribution. A 1-cm aperture device is experimentally demonstrated, but the structure is completely scalable. Theoretical results validate the design, and experimental results demonstrate precise control over the topological charge for both positive and negative values of orbital angular momentum. Remarkably, the conversion efficiency for the first topological charges is almost 100%. The reduction in efficiency of the higher-order modes has been explained theoretically, and it is not caused by design but by the PEDOT characteristics. The fabrication process is straightforward, as the high-resistivity layer may also be inhomogeneous. This work contributes significantly to the field by introducing a novel method for optical vortex generation. The simplicity of the fabrication process, high conversion efficiency, and ability to control the topological charge make this technique a promising avenue for future research and applications.

1. Introduction

The study of light's complex phase profiles, particularly helical wavefronts, has gained significant attention recently. When focused, these beams carry orbital angular momentum (OAM) that forms rings instead of points in a focal plane, leading to a wide range of applications spanning from laser processing [1–3], beam shaping [4], optical tweezers [5], atom manipulation [6], to free-space communications [7]. Moreover, the last ten years have seen rapid advancements in the overall field of optical vortices and OAM applications [8–21]. Several methods exist to obtain optical vortices; one of the most common methods is using spiral phase plates (SPPs) [22]. The helical surface is discretized into different refractive index steps, which generates the corresponding spatial phase profile. A fixed SPP is obtained by matching the refractive index to that of a target azimuthal phase dependence. They can be produced using techniques such as multi-stage vapour deposition processes, direct electron-beam writing, or metasurfaces [23]. Another option for obtaining optical vortices is using computer-generated holograms (CGHs) [24]. CGHs are computationally designed phase patterns that encode the necessary information to generate specific optical vortex structures. These holograms are used to manipulate the phase of the incident light, thereby creating a beam with the desired topological charge. The versatility of CGHs allows for the generation of various complex beam profiles, including those with diverse intensity distributions, by simply altering the phase pattern [25]. A computer-generated hologram can be displayed on a Spatial Light Modulator (SLM), or it can be printed onto a mask or film using lithography (in this case losing tunability). In the case of SLMs, they can dynamically display CGHs, modulating the phase of the incident light in real-time. However, SLMs do not inherently resolve all the issues associated with CGHs, such as diffraction efficiency (around 60%–85% [26]), poor fill factors < 40% [27] and potential aberrations introduced during phase modulation. For example, in [28], the authors demonstrate the generation of vortex lattices using spatial light

* Corresponding author at: CIBER de Bioingeniería, Biomateriales y Nanomedicina, Instituto de Salud Carlos III, 28029, Madrid, Spain.
E-mail address: algorrijf@unican.es (J.F. Algorri).

https://doi.org/10.1016/j.optlastec.2024.111849
Received 1 August 2024; Received in revised form 4 September 2024; Accepted 21 September 2024
Available online 5 October 2024

modulators (SLMs) with optimized phase patterns to produce high-quality structured light fields. This method allows for precise control over the lattice structure and the resulting light distribution. However, it is limited by the inherent diffraction efficiency and response time constraints associated with SLMs. Besides, [29] discusses the generation of vortex beams with complex intensity distributions using advanced holographic techniques. This approach achieves high-order vortex generation with improved control over the beam's properties, but it also faces challenges related to the complexity of the hologram design and the limitations of the optical setup. To solve these problems, multiple electrodes shaped like pie slices were proposed to generate a discretized SPP. The first proposal used 16 electrodes of Indium Tin Oxide (ITO) to generate the first two topological charges [30]. Subsequent proposals increased the number of devices, considerably reducing the efficiency though [31], or used spiral-shaped electrodes, resulting in a Spiral Diffractive Lens (SDL) [32]. Subsequently, other groups optimized the design by adding more control electrodes (e.g., 24 electrodes providing up to $l = 12$) [33,34]. One of the main problems with this technique is the requirement for complex voltage controllers.

Recently, this problem was solved using the transmission electrode technique. This technique, which has been previously demonstrated in several spatial light modulators [35,36] and lenses, e.g., cylindrical and Powell [37,38], axicons [35,39,40], aspherical [41–45], and arrays [46], was also proven for an optical vortex generator [47]. The device generated an almost continuous spiral phase profile (100 pie-slice electrodes distributed the voltage) that was completely reconfigurable using only two low-value voltages (up to $l = \pm 4$ were experimentally demonstrated employing a low-birefringence LC). Despite this, the sought-after continuous SPP was not achieved, and the problem of an unused central area in the middle due to the resolution limit of the lithographic fabrication process was still present, as can be observed in Fig. 2(c) of Ref. [47]. A continuous SPP would require a homogeneous layer that distributes the voltage across the active area completely and continuously from one contact to another. This was theoretically predicted in Ref. [48] by using two narrow stripe electrodes and a circular high resistivity layer. Still, this configuration would require a highly conducting ITO electrode (or a metallic electrode) for large apertures to avoid voltage drops from the contacts to the centre area. The PEDOT would have to be deposited only in the active area, making the fabrication process more complex.

In this context, the Sokova group demonstrated the feasibility of a modal spiral phase plate by adding the two narrow stripe electrodes to an LC focusator [49,50]. The high-resistivity layer was enclosed by 4 additional rectangular electrodes (thus leading to a total of 6 voltage sources to control the device), and the gap between stripe electrodes was free of the high-resistivity layer. This configuration allows for forming a phase delay similar to a phase spiral plate with an active area of 2 mm^2 [51,52]. As previously demonstrated with lenses [53,54], the modal technique is based on a high resistivity layer to distribute the voltage. To achieve this high resistivity, the layers are usually very thin; for this reason, homogeneity is very difficult to achieve in large-aperture areas. Besides, the fabrication of these devices is complex as the thickness has to be precisely controlled.

Currently, there is no experimental proof of the feasibility of using high-resistivity layers in an optical vortex generator for the two reasons mentioned above: the difficulty in achieving a high-resistivity layer homogeneous over a large area (> 1 cm) with a circular shape and the requirement of an ultra-high conducting ITO electrode or a metallic electrode that is difficult to obtain on glass. The present work solves these problems with a novel hybrid structure, constructively combining features from both the modal and transmission electrode techniques (trans-modal technique). This innovative structure can generate a continuous spiral phase profile completely reconfigurable using only two low voltages. This novel adaptive spiral phase plate (ASPP) has the potential to generate various positive and negative topological charges (up to $l = \pm 4$ are experimentally demonstrated here with a low-birefringence LC), reducing complexity and enhancing efficiency.

2. Structure and operation principle

The key component is a circular transmission electrode that generates a continuous voltage profile from one electric contact to another, as shown in the grey squares of Fig. 1(a). Subsequently, a series of stubs that extend from the periphery to the centre distribute the voltage throughout the active area. In Fig. 1(b), a simplification of the structure can be observed. As with the pie-slice electrode configuration commented before, there is a limit to the number of electrodes that can reach the centre due to the width of the stubs and the gap between them. To circumvent this issue, each stub has a different length, ensuring almost complete space utilization and enabling the electrodes to reach the centre. This is better shown in the details in Fig. 1(c), which is the real photograph of the chrome mask used in the photolithography process (the image has high resolution, so it can be zoomed). Each stub electrode fills the space between two adjacent stub electrodes until the gap between them reaches 10 μm; thanks to this, the maximum gap, namely without being covered by ITO, is 30 μm (a zoom can be made in Fig. 1(c) to observe this effect). As discussed, 1570 stub electrodes fill the active area to maximum achievable coverage, maintaining a distance of 10 μm between them (so as not to push the photolithography to resolution limits).

The second key component is the high-resistivity layer. This allows the electric field to be distributed continuously among the gaps without abrupt steps. Another way to see it is that these stub electrodes help the high-resistivity layer produce a continuous voltage profile despite its potential local inhomogeneities. We have chosen PEDOT:PSS material, a two-ionomer compound, as it is easy to deposit. PEDOT [Poly(3,4-ethylenedioxythiophene)] is a conducting polymer mixture that provides conductivity due to its conjugated polymer structure, allowing electron delocalization while PSS (polystyrene sulfonate), the second ionomer, is insulating. The core–shell structure, with conductive PEDOT cores surrounded by insulating PSS shells, leads to varying conductivity levels (10^{-2} to 10^{5} S/m). The conductivity can be significantly modified by manipulating the PEDOT to PSS ratio, e.g., by incorporating additives or dopants, and applying post-treatments like solvent or acid treatments that remove PSS and improve PEDOT morphology, the conductivity can be increased. Techniques such as layering and nanocomposites can also enhance its conductivity by improving PEDOT chain connectivity and reducing the PSS content.

The devices were fabricated by spin-coating a commercial dispersion of PEDOT mixed with a crosslinker to enhance film integrity and adhesion. The solvent used in the composition is water, with a PEDOT/PSS ratio of 1 : 6 w/w. The solid content ranges from 1.3 to 1.7 wt.%, and the work function is between 5.0 and 5.2 eV. The resistivity varies from 500 to 5000 Ω cm, while the sheet resistance exceeds 10^{6} Ω/sq, indicating low conductivity between 0.0002 and 0.002 S/cm. The particle size distribution shows a D90 of 100 nm and a D50 of 80 nm. The viscosity is between 5 and 12 mPa s, and the pH value ranges from 1.0 to 2.0. The solution is packaged in a 100 ml light-resistant bottle with a temperature indicator and should be stored at 3 to 5 °C.

The device comprises a pair of substrates coated with Indium Tin Oxide (ITO). Only one substrate is photolithographed with the transmission electrode pattern, as in Fig. 2(a). Fig. 2(b) illustrates an exploded-view schematic of the overall structure. The substrates are separated by a 50 μm thick spacer. The cavity formed in-between is occupied by a nematic liquid crystal (LC). The chosen LC is 6-CHBT, with a birefringence $\Delta n = 0.16$ [55]. The device is designed as an adaptive phase-only modulator and, therefore, does not require a molecular twist. Hence, a homogeneous alignment is made by a rubbing process. This is achieved by utilizing a polyimide alignment layer (PIA2000), rubbed parallel to the electrodes for the upper glass and in the opposite direction for the lower one.

The denoted voltage values V_1 and V_2 represent the applied voltage on the top electrodes. One of the advantages of the transmission

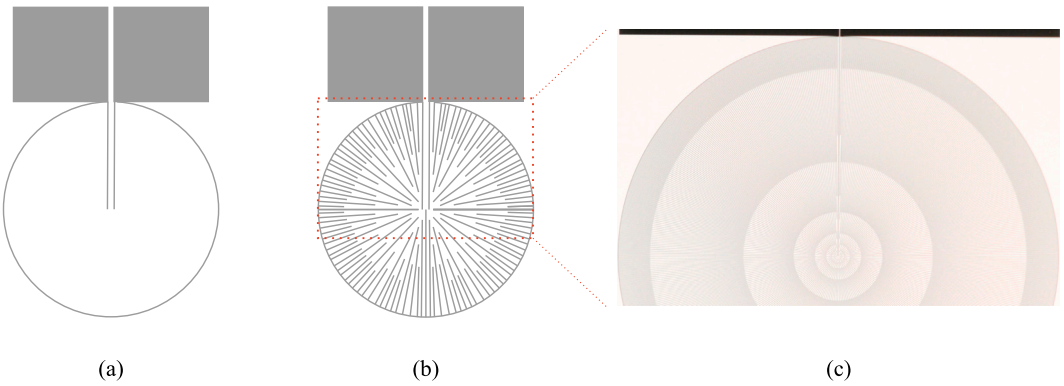

Fig. 1. (a) Schematic depiction of the circular transmission electrode and the two principal stubs that carry the voltage to the lens centre. (b) Schematic depiction of the complete electrode structure, where the transmission electrode and the stubs are evenly arranged to distribute the voltage. Note these drawings are not to scale. (c) Part of the chrome mask used in the photolithographic fabrication process.

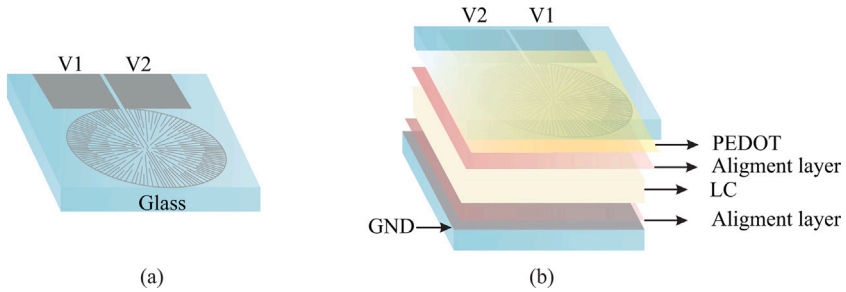

Fig. 2. Schematic depiction of the LC-tunable optical vortex generator and its constituent parts. (a) Detail of the top substrate electrode with the transmission electrode and stub structure patterned on an ITO layer. (b) Exploded-view depiction of the different layers comprising the device.

electrode technique is that the resistance from V_1 to V_2 is very high. The total voltage distribution is calculated numerically by means of the Finite Element Method (FEM), considering a static approach of the LC (constant dielectric anisotropy, ε_o and ε_e) and the entire structure. The first theoretical study is devoted to demonstrating the effect of the PEDOT layer in the structure. As can be observed in Fig. 3(a), the gaps between electrodes when no PEDOT layer is used produce a noticeable voltage gradient between stubs. This gradient is higher in the regions where the stubs are more separated and is produced by the capacitive effect of the LC (it should be noted that the ground electrode is connected in the other substrate). The lower the LC thickness, the more pronounced the voltage gradient, causing a considerable defect. Despite this, as demonstrated in Fig. 3(b), the PEDOT layer completely suppresses this problem, even with the lower conductivity (σ = 0.02 S/m). Moreover, using the lower conductivity produces a better voltage distribution in the stripe electrodes region, as demonstrated in the zoom image of Fig. 3(c). This figure reveals a negligible voltage step that can even be reduced by decreasing the PEDOT thickness. Instead, if we consider the higher conductivity of the PEDOT datasheet (σ = 0.2 S/m), there is a considerable voltage drop at the stripe electrode connected to contact V_2, resulting in a significant voltage step with the other stubs emanating from the periphery, see Fig. 3(d). This voltage drop can create a phase defect in the central area that might be observable. In order to analyse this effect, the results in Fig. 3(e) illustrate the voltage drop at the stub connected to V_2 (the inset indicates the corresponding position along the x-axis). The applied voltage at the contacts is an AC signal of 1 kHz with $V_1 = 2\ V_{\mathrm{RMS}}$ and $V_2 = 1\ V_{\mathrm{RMS}}$. Both the maximum and minimum conductivities of the PEDOT material are considered, along with several film thicknesses, thus spanning more than one order of magnitude in terms of the PEDOT film sheet conductance. As demonstrated in Ref. [56], the film thickness can be adjusted by altering the spin speed or by applying multiple layers. An inverse relationship between film thickness and spin speed was observed, with thicknesses ranging from 325 nm at 500 RPM to 60 nm at 5000 RPM. However, spin speeds below 500 RPM resulted in nonuniform films, while speeds exceeding 5000 RPM did not significantly reduce thickness. The electrical conductivity remained unaffected by spin speed, suggesting that morphological changes due to centrifugal forces did not influence conductivity. In the investigated case, the results show a notable difference for conductivity values varying from 0.2 S/m and 0.02 S/m. The latter case results in relatively low voltage drops, while the higher conductivity results in a voltage drop of 0.1 V_{RMS} at the minimum achievable thickness. This corresponds to almost a 2π radian phase shift for a 50 μm-thick LC layer. This effect is produced by the high resistivity layer between stripe electrodes, which produces current conduction between electrodes. Therefore, the lower the conductivity and thickness of the PEDOT layer, the better the device's performance. In this regard, maintaining the conductivity and thickness of the PEDOT layer low is also advantageous for reducing the current consumption and possible heating. As an example, considering the case of Fig. 3(d), the theoretical resistance (based on numerical simulations) is R = 55.6 kΩ, that for gradient voltages of 1 V_{RMS} it implies a current of only 18 μA_{RMS} and negligible heating.

3. Setup and experimental results

The optical system depicted in Fig. 4(a) was employed to measure the phase shift profile induced by the LC-ASPP. A collimated He-Ne laser (wavelength of 632.8 nm) is used as a light source. The ASPP is placed between crossed polarizers (+45°and −45°with respect to the sample), acting as a polarizer (P) and an analyzer (A) in order to measure the interference pattern between extraordinary and ordinary rays.

The interference pattern images are captured on a CCD using bi-convex lenses to resize the image. This approach reveals that the bright-dark transitions, each marking a 2π radian change, can be used

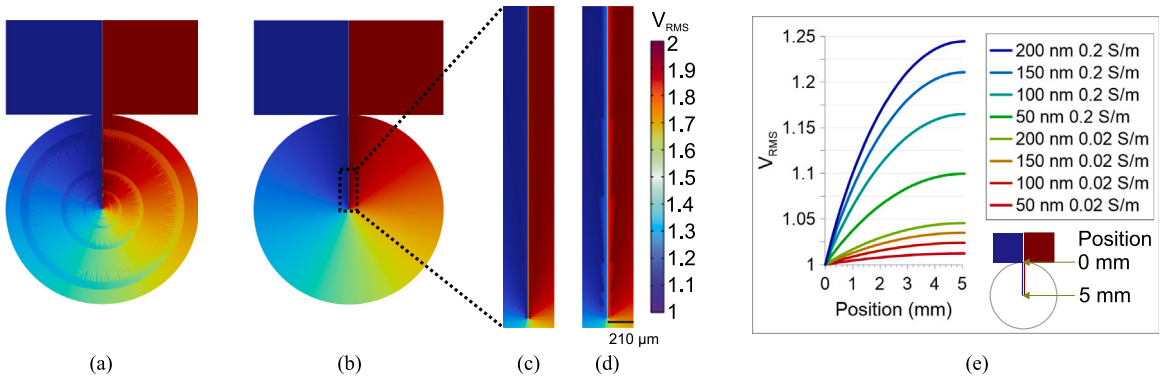

Fig. 3. (a) Structure without PEDOT: 2D voltage profile in the transmission electrode layer and gap between stubs, extracted from a numerical simulation of the whole 3D structure (b) Structure with PEDOT: 2D voltage profile in the PEDOT layer (t_{HR} = 100 nm and σ = 0.02 S/m). (c) Zoom for a PEDOT layer of t_{HR} = 100 nm and σ = 0.02 S/m. It can be observed that the voltage gradient is negligible for the latter case, so presumably, it will not have phase defects. (d) Zoom for a PEDOT layer of t_{HR} = 100 nm and σ = 0.2 S/m; due to the voltage drop at the electrode, there is an observable voltage gradient in this area. (e) Voltage drop at the stub that is connected to the V_2 electrode (the inset indicates the corresponding x-axis profile of the graph). Each line corresponds to a certain PEDOT layer thickness and conductivity.

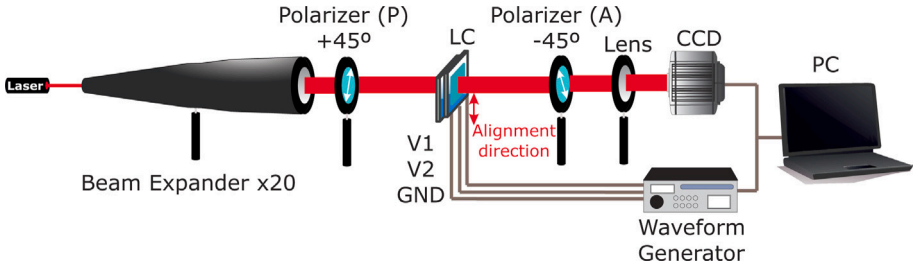

Fig. 4. Schematic of the optical system for measuring phase shift profiles and focal spot (by using only P polarizer parallel to the alignment layer). A diaphragm selects only a small region in the active central area of the device.

to calculate the topological charge. The setup for examining the ring focal spot is identical to that in Fig. 4, but it exclusively employs the P polarizer aligned parallel to the LC alignment layer (zero degrees). The same collimated He-Ne laser serves as the light source. When the light beam traverses a polarizer aligned with the liquid crystal director, it interacts with the LC effective refractive index. A key factor to consider is the linearity of the birefringence curve. Specifically, 6-CHBT displays an almost linear response between 1 and 2 V_{RMS}, with optimal linearity from 1 to 1.6 V_{RMS}, aligning with the threshold and saturation voltages, respectively [47]. Our experiments use the maximum range, which allows for some observable non-linearity at higher modes, thus slightly reducing the conversion efficiency in those cases.

The phase shift distribution is depicted in Fig. 5. The LC layer can generate eight distinct topological charges, specifically $l = \pm 1$ to ± 4. Here, l denotes the topological charge, which is determined by the number of phase changes per wavelength along the beam axis. The findings indicate that slight adjustments in voltage can result in significant changes in the phase shifts. It is crucial to note that multiples of 2π are required to create optical vortices. Furthermore, fine-tuning of the applied voltage allows the phase shift to be maintained at 2π (or a multiple thereof), even when the operation wavelength varies.

The distribution of light intensity at the focal spot provides valuable insights into the topological charge of an optical vortex. Fig. 6 illustrates the ring focal spot at various voltages for a wavelength of 632.8 nm, demonstrating precise control over the topological charge. Adjusting V_2 slightly enables the achievement of eight distinct modes. The diameter of the ring-shaped focal spot created by vortex light was estimated by calculating the distance between full-width half maximums of the outer part of the ring. For topological charges from $l = +1$ to $l = +4$, the diameters were estimated respectively as 250 µm, 310 µm, 375 µm and 440 µm. For higher topological charges, the defect in the stripe electrodes causes noticeable distortion in the rings. Additionally, this distortion is influenced by the non-linearity of the birefringence curve of the LC. Further research is necessary to address these issues, considering two potential solutions: (1) optimizing the PEDOT material to be less conductive and have thinner layers, and (2) improving the LC material to achieve higher birefringence with a more linear response.

The negative topological charge can be readily generated by swapping the voltages at V_1 and V_2, as depicted in Fig. 5; the phase is inverted. To demonstrate this effect two vortex cells are placed in cascade in the setup with the P polarizer aligned parallel to the LC alignment layer. One cell will generate a topological charge l_1 whereas the other l_2. The experiment combines the results of Fig. 6 for positive and negative values. The results for different combinations of topological charge generated by two cascade cells, a vortex generator (l_1) and a vortex analyser (l_2), are shown in Fig. 7. The vortex generator produces a topological charge from $l_1 = \pm 1$ to ± 4 whereas the analyser from $l_2 = +1$ to $+4$. The results are the arithmetic sum of the topological charge in each device, which generate a double topological charge when both are positive (l_{Tot} from 2 to 8) and zero when they have opposite signs (a Gaussian beam profile).

Finally, the setup for conversion efficiency measurements was similar to the one used in Fig. 4 for the ring focal spot. The difference, however, was substituting the CCD camera with a photodetector (PD). The pipeline for measurement included detecting the light intensity without the ASPP, with ASPP without voltage bias of the sample and with applied voltages that result in the generation of topological charges. The conversion efficiency for each charge l is calculated through Eq. (1), which expresses the percentage ratio between the output power of the biased device with respect to that in the rest case [47].

$$\mathrm{CE}_l = \frac{V_{\mathrm{PD}}(Q_l)}{V_{\mathrm{PD}}(\mathrm{ASPP}_{\mathrm{Off}})} \cdot 100\% \tag{1}$$

As can be observed in Table 1, almost 100% of conversion efficiency is obtained for topological charges 1 and 2. Higher topological charges,

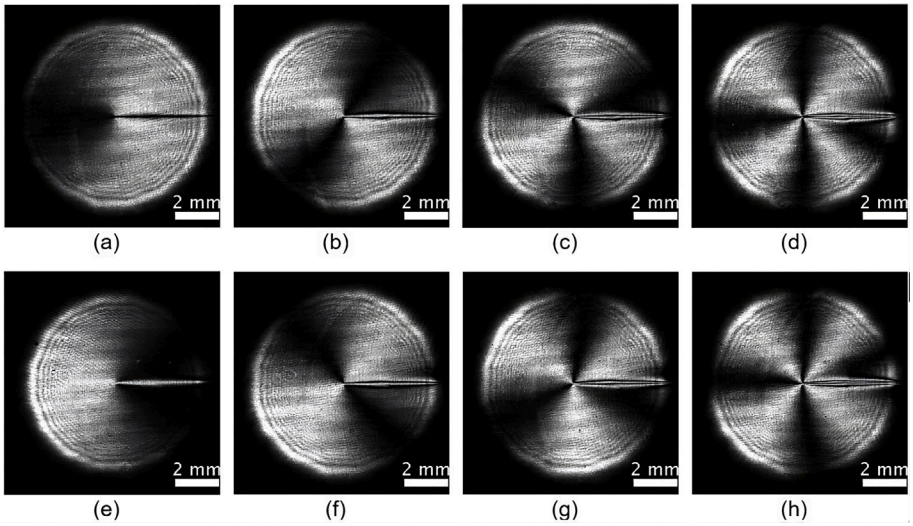

Fig. 5. Phase shift corresponding to different topological charges: (a) $l = 1 : V_1 = 1.56\ V_{RMS}$, $V_2 = 2.00\ V_{RMS}$, (b) $l = 2 : V_1 = 1.33\ V_{RMS}$, $V_2 = 2.00\ V_{RMS}$, (c) $l = 3 : V_1 = 1.11\ V_{RMS}$, $V_2 = 2.00\ V_{RMS}$, (d) $l = 4 : V_1 = 0.93\ V_{RMS}$, $V_2 = 2.00\ V_{RMS}$, (e) – (h) for $l = -1$ to $l = -4$ inverted voltages in V_1 and V_2 are applied.

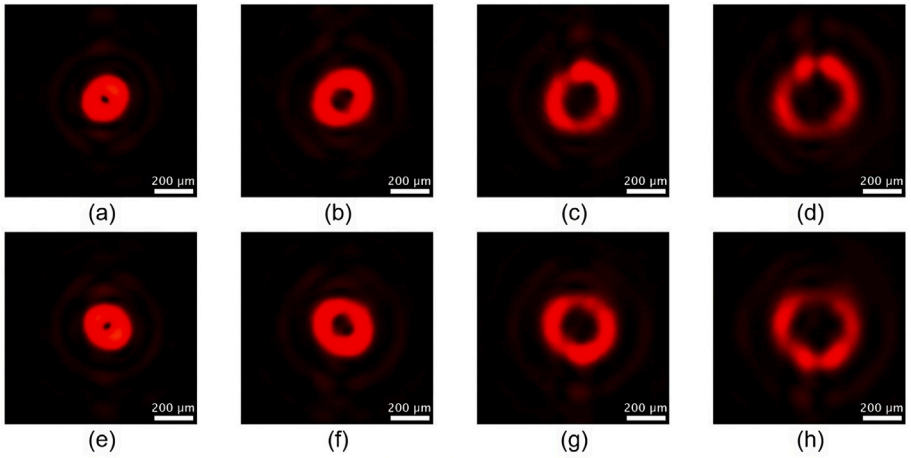

Fig. 6. Focal spot for different topological charges: (a) $l = 1 : V_1 = 1.56\ V_{RMS}$, $V_2 = 2.00\ V_{RMS}$, (b) $l = 2 : V_1 = 1.33\ V_{RMS}$, $V_2 = 2.00\ V_{RMS}$, (c) $l = 3 : V_1 = 1.11\ V_{RMS}$, $V_2 = 2.00\ V_{RMS}$, (d) $l = 4 : V_1 = 0.93\ V_{RMS}$, $V_2 = 2.00\ V_{RMS}$, (e) – (h) for $l = -1$ to $l = -4$ inverted voltages in V_1 and V_2 are applied.

such as $l = 4$, exhibit a lower conversion efficiency (around 98%) than lower topological charges like $l = 1$. This discrepancy can be attributed to the defect observed in the centre, as this technique will obtain almost 100% efficiency for all topological charges if the PEDOT layer and LC material are optimized. Despite this, these values are much higher than previous works [47]. It has to be noted that the cell's transmittance (the percentage ratio of the output power without voltage, '$ASPP_{Off}$', to the applied input laser power, 'Free Path'. This results in a transmittance of 86.3%.

Another important consideration is that while the 6CHBT has a birefringence of 0.16, alternative LC materials like TL296 (with Δn = 0.215 at 546 nm) [57] and NLC1929 (Δn = 0.3375 at 636 nm) [58] can be used. These materials offer substantially higher birefringence values, which could effectively double the ASPP capability, thereby doubling the potential range of topological charges the device can handle. Additionally, the phase shift is affected by other parameters such as the LC thickness and the wavelength of the incident light. The relationship between the LC layer thickness and the phase shift it produces is linear (for a fixed birefringence and operating wavelength), meaning that increasing the LC layer thickness enhances the phase shift encountered by incoming light. Combining these two effects, producing a continuous range of topological charges up to $l = \pm 16$ will be possible.

Table 1
Measured voltages at the photodiode for different topological charges. Note: The resolution of the photodiode measurements is 0.006 V (0.38%).

	V_{PD} (mV)	Conversion efficiency (%)
Free path	1,842	–
$ASPP_{Off}$	1.590	–
l_1	1.590	100.00
l_2	1.584	99.6
l_3	1.572	98.9
l_4	1.566	98.5
$-l_1$	1.590	100.0
$-l_2$	1.578	99.2
$-l_3$	1.560	98.1
$-l_4$	1.554	97.7

4. Conclusions

This study has successfully demonstrated a novel hybrid structure for generating optical vortices with high precision and efficiency. The large aperture optical vortex generator combines the modal and transmission electrode techniques to facilitate precise control over topological charges ranging from $l = \pm 1$ to ± 4. The device showcases

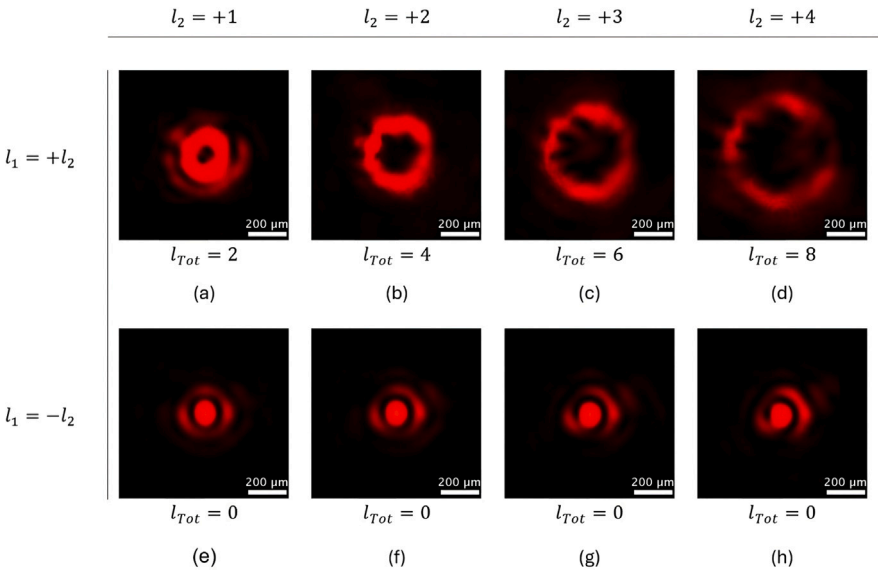

Fig. 7. Focal spot for different combinations of topological charges generated by two cascade cells, a vortex generator (l_1) and a vortex analyser (l_2). The vortex generator produces a topological charge from $l_1 = \pm 1$ to ± 4. The vortex analyser always had a positive topological charge with a value ranging from $l_2 = +1$ to $+4$. The results are for topological charges at the generator and analyser as follows: (a) $l_1 = +1, l_2 = +1$, (b) $l_1 = +2, l_2 = +2$, (c) $l_1 = +3, l_2 = +3$, (d) $l_1 = +4, l_2 = +4$, (e) $l_1 = -1, l_2 = +1$, (f) $l_1 = -2, l_2 = +2$, (g) $l_1 = -3, l_2 = +3$, (h) $l_1 = -4, l_2 = +4$. The total topological charge at the output of the two cells is the arithmetic sum.

nearly perfect conversion efficiency for lower topological charges, with a slightly reduced efficiency for higher orders due to inherent material characteristics, such as the non-perfect linearity of the effective birefringence curve. Experimental results validate the theoretical predictions, confirming the device's capability to control both positive and negative topological charges effectively. Minor voltage adjustments result in substantial modifications in phase shifts, demonstrating the fine control achievable with this setup. The high resistivity layer contributes significantly to the continuous voltage distribution by mitigating abrupt voltage steps that could otherwise distort the optical vortices. Future work will focus on refining the PEDOT layer's conductivity to further enhance the device's efficiency across all topological charges. Additionally, exploring higher birefringence materials could extend the linear operation region, broadening the application spectrum. This research lays a solid foundation for developing more advanced optical vortex generators, promising significant advancements in fields such as optical tweezers, free-space communications, and beyond. For example, the results obtained in this work can be extended to other areas of singular optics [59,60]. The concept of the fine structure of optical vortices [61] can be applied to the study of the properties of topological charges in anisotropic media and optical fibres [62], which can be used to analyse the properties of spin and orbital angular momentum in free space, anisotropic media, and weakly turbulent atmospheric media. The results can also be used in areas related to polarization and phase profilometry of surfaces. Further research in this direction may lead to the development of new types of optical devices and systems based on the unique properties of singular beams in anisotropic and gyrotropic media.

CRediT authorship contribution statement

A. Walewska: Writing – review & editing, Investigation. **N. Bennis:** Writing – review & editing, Supervision, Resources, Investigation. **T. Jankowski:** Writing – review & editing, Investigation. **P. Morawiak:** Writing – review & editing, Investigation. **D.C. Zografopoulos:** Writing – review & editing, Software, Investigation. **M. Filipiak:** Writing – review & editing, Investigation. **M. Słowikowski:** Writing – review & editing, Investigation. **A. Cobo:** Writing – review & editing, Resources, Investigation. **J.F. Algorri:** Writing – review & editing, Writing – original draft, Supervision, Project administration, Investigation, Conceptualization.

Declaration of competing interest

The authors declare that they have no known competing financial interests or personal relationships that could have appeared to influence the work reported in this paper.

Data availability

Data will be made available on request.

Acknowledgements

The authors would like to thank Prof. Ignacio Moreno for his helpful suggestions. J.F.A. acknowledges the support of the project RYC2022-035279-I funded by MCIN/AEI/10.13039/501100011033, Spain and FSE+. Also, by projects TED2021-130378B-C21 and PID2022-137269OB-C22 funded by MCIN/ AEI /10.13039/501100011033, Spain and by FEDER, Spain "A way to make Europe". N. Bennis also acknowledges research project UGB 22-725 (Military University of Technology). D.C.Z. acknowledges the support of the project PRIN-2022 ALPHA (202288M84C) "ALl-dielectric resonant metasurfaces enhancing PHoton emission phenomenA" (CUP Master:D53D23001060006, CUP:B53D2300233 0006), Italian Ministry of University and Research (MUR), financed by the European Union, Next Generation EU. Finally, it has to be noted that this research was carried out on devices co-funded by the Warsaw University of Technology, Poland within the Excellence Initiative: Research University (IDUB) programme.

References

[1] J. Hamazaki, R. Morita, K. Chujo, Y. Kobayashi, S. Tanda, T. Omatsu, Optical-vortex laser ablation, Opt. Express 18 (3) (2010) 2144–2151.
[2] K. Toyoda, K. Miyamoto, N. Aoki, R. Morita, T. Omatsu, Using optical vortex to control the chirality of twisted metal nanostructures, Nano Lett. 12 (7) (2012) 3645–3649.
[3] T. Omatsu, K. Miyamoto, K. Toyoda, R. Morita, Y. Arita, K. Dholakia, A new twist for materials science: The formation of chiral structures using the angular momentum of light takashige, Adv. Opt. Mater. 7 (14) (2019) 1801672.
[4] M. Padgett, R. Bowman, Tweezers with a twist, Nat. Photonics 5 (6) (2011) 343–348, http://dx.doi.org/10.1038/nphoton.2011.81.

[5] K. Ladavac, D.G. Grier, Microoptomechanical pumps assembled and driven by holographic optical vortex arrays, Opt. Express 12 (6) (2004) 1144, http://dx.doi.org/10.1364/OPEX.12.001144.

[6] J.W.R. Tabosa, D.V. Petrov, Optical pumping of orbital angular momentum of light in cold cesium atoms, Phys. Rev. Lett. 83 (24) (1999) 4967–4970, http://dx.doi.org/10.1103/PhysRevLett.83.4967, URL http://link.aps.org/doi/10.1103/PhysRevLett.83.4967.

[7] J. Wang, J.-Y. Yang, I.M. Fazal, N. Ahmed, Y. Yan, H. Huang, Y. Ren, Y. Yue, S. Dolinar, M. Tur, A.E. Willner, Terabit free-space data transmission employing orbital angular momentum multiplexing, Nat. Photonics 6 (7) (2012) 488–496, http://dx.doi.org/10.1038/nphoton.2012.138.

[8] N. Bozinovic, Y. Yue, Y. Ren, M. Tur, P. Kristensen, H. Huang, A.E. Willner, S. Ramachandran, Terabit-scale orbital angular momentum mode division multiplexing in fibers, Science 340 (6140) (2013) 1545–1548, http://dx.doi.org/10.1126/science.1237861, URL http://www.sciencemag.org/content/340/6140/1545.

[9] R. Fickler, G. Campbell, B. Buchler, P.K. Lam, A. Zeilinger, Quantum entanglement of angular momentum states with quantum numbers up to 10 010, Proc. Natl. Acad. Sci. USA 113 (2016) 13642–13647.

[10] R.C. Devlin, A. Ambrosio, N.A. Rubin, J.P.B. Mueller, F. Capasso, Arbitrary spin-to–orbital angular momentum conversion of light, Science 358 (2017) 896–901.

[11] T. Stav, A. Faerman, E. Maguid, D. Oren, V. Kleiner, E. Hasman, M. Segev, Quantum entanglement of the spin and orbital angular momentum of photons using metamaterials, Science 361 (2018) 1101–1104.

[12] F. Kong, C. Zhang, F. Bouchard, Z. Li, G.G. Brown, D.H. Ko, T.J. Hammond, L. Arissian, R.W. Boyd, E. Karimi, P.B. Corkum, Controlling the orbital angular momentum of high harmonic vortices, Nature Commun. 8 (2017) 14970.

[13] D. Gauthier, P.R. Ribič, G. Adhikary, A. Camper, C. Chappuis, R. Cucini, L.F. DiMauro, G. Dovillaire, F. Frassetto, R. Géneaux, P. Miotti, L. Poletto, B. Ressel, C. Spezzani, M. Stupar, T. Ruchon, G.D. Ninno, Tunable orbital angular momentum in high-harmonic generation, Nature Commun. 8 (2017) 14971.

[14] J.C.T. Lee, S.J. Alexander, S.D. Kevan, S. Roy, B.J. McMorran, Laguerre–gauss and hermite–gauss soft x-ray states generated using diffractive optics, Nat. Photonics 13 (2019) 205–209.

[15] Z. Xie, T. Lei, F. Li, H. Qiu, Z. Zhang, H. Wang, C. Min, L. Du, Z. Li, X. Yuan, Ultra-broadband on-chip twisted light emitter for optical communications, Light Sci. Appl. 7 (2018) 18001.

[16] N.C. Zambon, P. St-Jean, M. Milićević, A. Lemaître, A. Harouri, L.L. Gratiet, O. Bleu, D.D. Solnyshkov, G. Malpuech, I. Sagnes, S. Ravets, A. Amo, J. Bloch, Optically controlling the emission chirality of microlasers, Nat. Photonics 13 (2019) 283–288.

[17] L. Rego, K.M. Dorney, N.J. Brooks, Q.L.N. andChen Ting Liao, J.S. Román, D.E. Couch, A. Liu, E. Pisanty, C. Hernández-García, Generation of extreme-ultraviolet beams with time-varying orbital angular momentum, Science 364 (6447) (2019).

[18] H.H. Fan, Y.P. Tai, H.H. Li, X.Z. Li, Q.W. Zhan, Epicycle-model-guided arbitrary shaped customization of structured light, Appl. Phys. Lett. 122 (23) (2023) 231104, http://dx.doi.org/10.1063/5.0147002.

[19] L. Zhu, Y. Tai, H. Li, H. Hu, X. Li, Y. Cai, Y. Shen, Multidimensional optical tweezers synthetized by rigid-body emulated structured light, Photon. Res. 11 (9) (2023) 1524–1534, http://dx.doi.org/10.1364/PRJ.490103.

[20] M.A. Geday, M. Caño-García, J.M. Otón, X. Quintana, Adaptive spiral diffractive lenses—lenses with a twist, Adv. Opt. Mater. 8 (23) (2020) 2001199, http://dx.doi.org/10.1002/adom.202001199.

[21] K. i. Yuyama, H. Kawaguchi, R. Wei, T. Omatsu, Fabrication of an array of hemispherical microlasers using optical vortex laser-induced forward transfer, ACS Photonics (2023) http://dx.doi.org/10.1021/acsphotonics.3c01005.

[22] M.W. Beijersbergen, R.P.C. Coerwinkel, M. Kristensen, J.P. Woerdman, Helical-wavefront laser beams produced with a spiral phaseplate, Opt. Commun. 112 (6) (1994) 321–327.

[23] X. Wang, Z. Nie, Y. Liang, J. Wang, T. Li, B. Jia, Recent advances on optical vortex generation, Nanophotonics 7 (9) (2018) 1533–1556, http://dx.doi.org/10.1515/nanoph-2018-0072.

[24] N.R. Heckenberg, R. McDuff, C.P. Smith, A.G. White, Generation of optical phase singularities by computer-generated holograms, Opt. Lett. 17 (3) (1992) 221, http://dx.doi.org/10.1364/OL.17.000221.

[25] I. Zeylikovich, H.I. Sztul, V. Kartazaev, T. Le, R.R. Alfano, Ultrashort Laguerre-Gaussian pulses with angular and group velocity dispersion compensation, Opt. Lett. 32 (14) (2007) 2025, http://dx.doi.org/10.1364/OL.32.002025.

[26] A. Forbes, A. Dudley, M. McLaren, Creation and detection of optical modes with spatial light modulators, Adv. Opt. Photonics 8 (2) (2016) 200.

[27] J.M.O. Sanchez, J. Pereiro-García, X. Quintana, M. Caño-García, E. Otón, M.A. Geday, Optimizing tunable lc devices with twisted light, 2023, http://dx.doi.org/10.20944/preprints202311.0668.v1, Preprints.

[28] Y. Wang, H. Ma, Y. Tai, X. Li, Generation of discrete higher-order optical vortex lattice at focus, Opt. Lett. 48 (17) (2023) 4464–4467, http://dx.doi.org/10.1364/OL.497995.

[29] X. Qin, H. Zhang, M. Tang, Y. Zhou, Y. Tai, X. Li, Switchable hybrid-order optical vortex lattice, Opt. Lett. 49 (9) (2024) 2213–2216, http://dx.doi.org/10.1364/OL.515906.

[30] D. Ganic, X. Gan, M. Gu, M. Hain, S. Somalingam, S. Stankovic, T. Tschudi, Generation of doughnut laser beams by use of a liquid-crystal cell with a conversion efficiency near 100%, Opt. Lett. 27 (15) (2002) 1351–1353, http://dx.doi.org/10.1364/OL.27.001351.

[31] B. Wang, M. Ye, S. Sato, Lens of electrically controllable focal length made by a glass lens and liquid-crystal layers, Appl. Opt. 43 (17) (2004) 3420–3425.

[32] J. Albero, P. Garcia-Martinez, N. Bennis, E. Oton, B. Cerrolaza, I. Moreno, J.A. Davis, Liquid crystal devices for the reconfigurable generation of optical vortices, J. Lightwave Technol. 30 (18) (2012) 3055–3060.

[33] M. Caño-García, X. Quintana, J.M. Otón, M.A. Geday, Dynamic multilevel spiral phase plate generator, Sci. Rep. 8 (1) (2018) 15804, http://dx.doi.org/10.1038/s41598-018-34041-2.

[34] J. Pereiro-García, M. García-de Blas, M. Geday, et al., Flat variable liquid crystal diffractive spiral axicon enabling perfect vortex beams generation, Sci. Rep. 13 (2023) 2385, http://dx.doi.org/10.1038/s41598-023-29164-0.

[35] J.F. Algorri, D. Zografopoulos, A. Spadlo, L. Rodríguez-cobo, L.R. Jaroszewicz, J.M. Sánchez-pena, J.M. López-Higuera, Multifunctional light beam control device by stimuli-responsive liquid crystal micro-grating structures, Sci. Rep. 10 (2020) 13806, http://dx.doi.org/10.1038/s41598-020-70783-8.

[36] Z. Zemska, T. Galstian, Simple electrically tunable liquid crystal spatial phase modulator, Opt. Express 31 (4) (2023) 5388–5398, http://dx.doi.org/10.1364/OE.483736.

[37] J.F. Algorri, P. Morawiak, D.C. Zografopoulos, N. Bennis, A. Spadlo, L. Rodriguez-Cobo, L.R. Jaroszewicz, J.M. Sanchez-Pena, J.M. Lopez-Higuera, Cylindrical and Powell liquid crystal lenses with positive-negative optical power, IEEE Photonics Technol. Lett. 32 (17) (2020) 1057–1060, http://dx.doi.org/10.1109/lpt.2020.3011673.

[38] W. Feng, Z. Liu, M. Ye, Positive-negative tunable cylindrical liquid crystal lenses, Optik 266 (2022) 169613, http://dx.doi.org/10.1016/j.ijleo.2022.169613.

[39] J.F. Algorri, P. Morawiak, N. Bennis, D.C. Zografopoulos, V. Urruchi, L. Rodríguez-Cobo, L.R. Jaroszewicz, J.M. Sánchez-Pena, J.M. López-Higuera, Positive-negative tunable liquid crystal lenses based on a microstructured transmission line, Sci. Rep. 10 (1) (2020) 10153, http://dx.doi.org/10.1038/s41598-020-67141-z.

[40] J. Stevens, T. Galstian, Electrically tunable liquid crystal lens with a serpentine electrode design, Opt. Lett. 47 (4) (2022) 910–912, http://dx.doi.org/10.1364/OL.447853.

[41] N. Bennis, T. Jankowski, P. Morawiak, A. Spadlo, D.C. Zografopoulos, J.M. Sánchez-Pena, J.M. López-Higuera, J.F. Algorri, Aspherical liquid crystal lenses based on a variable transmission electrode, Opt. Express 30 (8) (2022) 12237–12247, http://dx.doi.org/10.1364/OE.451292.

[42] J.F. Algorri, D.C. Zografopoulos, L. Rodríguez-Cobo, J.M. Sánchez-Pena, J.M. López-Higuera, Engineering aspheric liquid crystal lenses by using the transmission electrode technique, Crystals 10 (9) (2020) 835, http://dx.doi.org/10.3390/CRYST10090835, URL https://www.mdpi.com/2073-4352/10/9/835/htm https://www.mdpi.com/2073-4352/10/9/835.

[43] A. Pusenkova, O. Sova, T. Galstian, Electrically variable liquid crystal lens with spiral electrode, Opt. Commun. 508 (2022) 127783, http://dx.doi.org/10.1016/j.optcom.2021.127783, URL https://www.sciencedirect.com/science/article/pii/S0030401821009585.

[44] W. Feng, Z. Liu, H. Liu, M. Ye, Design of tunable liquid crystal lenses with a parabolic phase profile, Crystals 13 (1) (2023) http://dx.doi.org/10.3390/cryst13010008.

[45] W. Feng, Z. Liu, M. Ye, Liquid crystal lens with a shiftable optical axis, Opt. Express 31 (10) (2023) 15523–15536, http://dx.doi.org/10.1364/OE.488844.

[46] W. Feng, Z. Liu, M. Ye, Liquid crystal lens array with positive and negative focal lengths, Opt. Express 30 (16) (2022) 28941–28953, http://dx.doi.org/10.1364/OE.464526.

[47] T. Jankowski, N. Bennis, P. Morawiak, D. Zografopoulos, A. Pakuła, M. Filipiak, M. Słowikowski, J. López-Higuera, J. Algorri, Optical vortices by an adaptive spiral phase plate, Opt. Laser Technol. 176 (2024) 111029, http://dx.doi.org/10.1016/j.optlastec.2024.111029.

[48] J.F. Algorri, V. Urruchi, B. Garcia-Camara, J.M. Sanchez-Pena, Generation of optical vortices by an ideal liquid crystal spiral phase plate, IEEE Electron Device Lett. 35 (8) (2014) 856–858, http://dx.doi.org/10.1109/LED.2014.2331339.

[49] S.P. Kotova, V.V. Patlan', S.A. Samagin, V.V. Patlan, S.A. Samagin, Tunable liquid-crystal focusing device. 1. Theory, Quantum Electron. 41 (1) (2011) 58–64, http://dx.doi.org/10.1070/QE2011v041n01ABEH014406.

[50] S.P. Kotova, V.V. Patlan, S.A. Samagin, Tunable liquid-crystal focusing device. 2. Experiment, Quantum Electron. 41 (1) (2011) 65–70, http://dx.doi.org/10.1070/QE2011v041n01ABEH014407.

[51] S.P. Kotova, A.M. Mayorova, S.A. Samagin, Formation of ring-shaped light fields with orbital angular momentum using a modal type liquid crystal spatial modulator, J. Opt. 20 (5) (2018) 055604, http://dx.doi.org/10.1088/2040-8986/aab8bb.

[52] S. Kotova, A. Mayorova, K. Efimova, S. Samagin, Tunable modal liquid crystal spiral phase plate, in: 2018 International Conference Laser Optics, ICLO, 2018, p. 196, http://dx.doi.org/10.1109/LO.2018.8435893.

[53] A.F. Naumov, M.Y. Loktev, I.R. Guralnik, G.V. Vdovin, Liquid-crystal adaptive lenses with modal control, Opt. Lett. 23 (13) (1998) 992–994, http://dx.doi.org/10.1364/OL.23.000992.

[54] A.F. Naumov, G.D. Love, M.Y. Loktev, F.L. Vladimirov, Control optimization of spherical modal liquid crystal lenses, Opt. Express 4 (9) (1999) 344–352, URL http://www.ncbi.nlm.nih.gov/pubmed/19396291.

[55] R. Dabrowski, J. Dziaduszek, T. Szczucinski, 4-/trans-4'-n-alkylcyclohexzyl/isothiocyanatobenzenes a new class of low-melting stable nematics, Mol. Cryst. Liquid Cryst. 102 (Lett) (5) (1984) 155–160, http://dx.doi.org/10.1080/01406568408072065.

[56] G. Dijk, H.J. Ruigrok, R.P. O'Connor, Influence of pedot:pss coating thickness on the performance of stimulation electrodes, Adv. Mater. Interf. 7 (16) (2020) 2000675, http://dx.doi.org/10.1002/admi.202000675.

[57] J.F. Algorri, B. García-Cámara, A. García-García, V. Urruchi, J.M. Sánchez-Pena, Fiber optic temperature sensor based on amplitude modulation of metallic and semiconductor nanoparticles in a liquid crystal mixture, J. Lightwave Technol. 33 (12) (2015) 2451–2455, http://dx.doi.org/10.1109/JLT.2015.2396357.

[58] N. Bennis, T. Jankowski, O. Strzezysz, A. Pakuła, D.C. Zografopoulos, P. Perkowski, J.M. Sánchez-Pena, J.M. López-Higuera, J.F. Algorri, A high birefringence liquid crystal for lenses with large aperture, Sci. Rep. 12 (1) (2022) 14603, http://dx.doi.org/10.1038/s41598-022-18530-z.

[59] Y. Egorov, A. Rubass, Spin–orbit coupling in quasi-monochromatic beams, Photonics 10 (3) (2023) http://dx.doi.org/10.3390/photonics10030305.

[60] Y. Egorov, A. Rubass, Gyrotropic crystals as a basis for creation of helical polychromatic singular beams, Photonics 10 (9) (2023) http://dx.doi.org/10.3390/photonics10091044.

[61] Y. Egorov, A. Rubass, Fine structure of optical vortices in linearly polarized Laguerre–Gaussian beams in oblique beams propagating a uniaxial crystal, Photonics 10 (6) (2023) http://dx.doi.org/10.3390/photonics10060684.

[62] Y. Egorov, A. Rubass, Polarization structure of optical vortices in inclined Laguerre-Gaussian beams passed through a uniaxial crystal, J. Opt. Soc. Amer. A 41 (6) (2024) 1000–1008, http://dx.doi.org/10.1364/JOSAA.523057.